Surveys in Geophysics
https://doi.org/10.1007/s10712-023-09782-z

Reflection and Transmission of Inhomogeneous Plane Waves in Thermoporoelastic Media

Wanting Hou[1] · **Li-Yun Fu**[1,2] · **José M. Carcione**[3,4]

Received: 14 October 2022 / Accepted: 6 March 2023

Abstract
We study the reflection and transmission (*R*/*T*) characteristics of inhomogeneous plane waves at the interface between two dissimilar fluid-saturated thermoporoelastic media at arbitrary incidence angles. The *R*/*T* behaviors are formulated based on the classic Lord–Shulman (LS) and Green–Lindsay (GL) heat-transfer models as well as a generalized LS model, respectively. The latter results from different values of the Maxwell-Vernotte-Cattaneo relaxation times. These thermoporoelastic models can predict three inhomogeneous longitudinal (P1, P2, and T) waves and one shear (S) wave. We first compare the LS and GL models for the phase velocities and attenuation coefficients of plane waves, where the homogeneous wave has a higher velocity but weaker thermal attenuation than the inhomogeneous wave. Considering the oil–water contact, we investigate *R*/*T* coefficients associated with phase angles and energy ratios, which are formulated in terms of incidence and inhomogeneity angles, with the latter having a significant effect on the interference energy. The proposed thermoporoelastic *R*/*T* model predicts different energy partitions between the P and S modes, especially at the critical angle and near grazing incidence. We observe the anomalous behavior for an incident P wave with the inhomogeneity angle near the grazing incidence. The energy partition at the critical angle is mainly controlled by relaxation times and boundary conditions. Beyond the critical angle, the energy flux predicted by the Biot poroelastic and LS models vanishes vertically, becoming the opposite for the GL and generalized LS models. The resulting energy flux shows a good agreement with the *R*/*T* coefficients, and they are well proven by the conservation of energy, where the results are valuable for the exploration of thermal reservoirs.

Keywords Thermoporoelastic *R*/*T* coefficients · Inhomogeneous plane waves · Energy partitions · Inhomogeneity angle · Critical angle

✉ Li-Yun Fu
lfu@upc.edu.cn

[1] Key Laboratory of Deep Oil and Gas, China University of Petroleum (East China), Qingdao 266580, China

[2] Laboratory for Marine Mineral Resources, Qingdao National Laboratory for Marine Science and Technology, Qingdao 266071, China

[3] National Institute of Oceanography and Applied Geophysics – INOGS, Trieste 34010, Italy

[4] Hohai University, Nanjing 210098, China

Published online: 23 April 2023

Article Highlights

- We study the characteristics of an inhomogeneous plane wave incident on the interface separated by two dissimilar fluid-saturated thermoporoelastic media at arbitrary incidence angle
- We compare the phase velocities and attenuation coefficients of plane waves for the Lord-Shulman (LS) and Green-Lindsay (GL) models, which depend on the inhomogeneity of the waves
- The influence of theory, inhomogeneity angle and the type of incident wave are considered in the numerical analysis

1 Introduction

The study of reflection and transmission of plane elastic waves at an interface separating two thermoelastic fluid-saturated porous media has practical significance in engineering structures, geothermal, and exploration geophysics (e.g, Deresiewicz 1960; Fu 2012; Abouelregal and Marin 2020). In geophysical prospecting, the effect of temperature on the petrophysical properties of reservoirs is crucial for hydrocarbon production (Fu 2017). The poroelastic *R*/*T* theory has been extensively explored (e.g., Santos et al. 1992; Gurevich et al. 2004; Carcione and Tinivella 2000; Sharma and Kumar 2011; Corredor et al. 2014; Markov et al. 2019), and extended to double-porosity media (Ba et al. 2011) to account for the effect of local fluid flow (Guo and Gurevich 2020). In this study, we further extend the poroelastic *R*/*T* model to thermoelastic media.

Thermoelasticity extends the classical elastic theory by coupling the deformation and temperature. From the mathematical and essential point of view, it is analogous to the mode of poroelasticity (Biot 1956; Deresiewicz 1957), but has an unphysical solution with infinite velocities as a function of frequency because of the classical parabolic-type equation of heat conduction. The unphysical behavior can be avoided by introducing a relaxation time into the heat equation, yielding a hyperbolic-heat-transfer differential equation (Lord and Shulman 1967). The Lord–Shulman (LS) thermoelasticity has been applied to numerical simulations to investigate the effect of thermophysical properties on wave propagation in nonporous media (Carcione et al. 2019a; Wang et al. 2020b; Hou et al. 2021), predicting a classical P wave, a slow P diffusive wave (T mode), and an S wave, where the existence of the T wave has been observed in experimentally in solid helium (Ackerman et al. 1966), NaF crystals (McNelly et al. 1970; Jackson et al. 1970) and graphite (Humberman et al. 2019). Green and Lindsay (1972) (Green–Lindsay or GL theory) propose an alternative generalization by using two relaxation times, considering the influence of temperature gradients. A comprehensive review identifies existing mistakes and flaws in previous studies about the thermoelastic *R*/*T* of plane elastic waves, especially on inhomogeneous plane waves in thermoelastic media. Based on the thermoelastic *R*/*T* for wave propagation in multilayered media (Hou et al. 2022a), Hou et al. (2023) develop a thermoelastic AVO method for seismic exploration of superdeep high-temperature oil/gas resources.

The LS thermoelasticity has been extended to porous media by incorporating Biot poroelasticity to describe wave dissipation due to fluid and heat flow (e.g., Noda 1990; Nield and Bejan 2006; Sharma 2008). The LS thermoporoelasticity theory can predict

the presence of both Biot and thermal slow P waves, besides the classical P and S waves. Numerical simulations by the Fourier pseudospectral method (Carcione et al. 2019a) show that the conversion between the Biot to thermal modes leads to mesoscopic energy attenuation. Wei et al. (2020) develop a frequency-domain Green's function as a displacement-temperature solution of LS thermoporoelasticity to investigate the effect of fluid viscosity and thermophysical properties. Based on the Biot-Rayleigh double-porosity theory (Ba et al. 2011), Li et al. (2022) extend the LS thermoporoelasticity to the case of double porosity by taking into account both the local heat/fluid flows in two types of pores. The double-porosity thermoporoelasticity theory can be used to develop a coupled THM thermoelastic model (Li et al. 2023) for the cyclic recovery of fractured-vuggy thermal reservoirs. Zhang et al. (2022) analyze the significance of thermal radiation on the hybrid nanofluid based on the generalized thermoelasticity model. For the *R*/*T* phenomena of thermoporoelastic waves we concern mostly, Wei et al. (2016) formulate an *R*/*T* model of lossless P-wave incidence at the interface between thermoelastic and thermoporoelastic media. Sharma (2018) addresses a similar problem but considers an inhomogeneous incident wave. The effects of the thermal parameters on dispersion (Zhou et al. 2019) and *R*/*T* amplitudes (Liu et al. 2021) are discussed for homogeneous plane waves in unsaturated thermoporoelastic media. Wang et al. (2021) and Liu et al. (2022) study the reflection of plane waves at the free surface of thermoporoelastic media. The former compares the LS, GL, and generalized LS models for the phase velocity and attenuation of inhomogeneous plane waves, while the latter focuses on the influence of thermophysical parameters on homogeneous behavior in unsaturated media.

In this study, we follow Wang et al. (2021) to analyze the *R*/*T* coefficients of inhomogeneous plane waves at the interface between two dissimilar fluid-saturated thermoporoelastic media. Based on the generalized Snell law for temperature and heat flux continuities across the interface, we formulate the *R*/*T* coefficients of inhomogeneous plane waves using the LS, GL, and generalized LS thermoporoelastic models, respectively. The propagation and attenuation directions do not coincide due to wave inhomogeneity. We investigate the effect of incidence angle, inhomogeneity angle, and type of incident wave on the velocity and attenuation. We discuss the effect of relaxation times on the thermoporoelastic attenuation by comparing with the classical Biot theory and generalized LS model.

2 Thermoporoelasticity

2.1 Governing Equations

Considering a thermally homogeneous porous solid saturated with a viscous compressible fluid, implying the whole aggregate assumes isotropic. The grain of solid is characterized by its bulk modulus by K_s and density ρ_s. The pore fluid is characterized by its thermoelasticity coefficient β_f, bulk modulus K_f, viscosity η, and density ρ_f. The rock frame is characterized by its bulk modulus K_{m}, Lamé constants μ and λ, porosity $\bar{\phi}$, permeability $\bar{\kappa}$, structure factor tortuosity $\mathcal{T}$, and density $\rho = (1-\bar{\phi})\rho_s + \bar{\phi}\rho_f$. The bulk thermal property is characterized by its thermoelasticity coefficient β, the specific heat of the unit volume in the absence of deformation c, thermal conductivity $\bar{\gamma}$, relaxation time τ, and absolute temperature T_0. With u and w representing the average solid and fluid displacements of the medium and T denoting the increment of temperature above a reference T_0 for the state of zero stress and strain, the

relative compact equations for the displacement components and temperature fluctuation are defined from Eq. (A.3) as (Carcione et al. 2019b; Wang et al. 2021)

$$
\begin{aligned}
&(\lambda+\mu+\bar{\alpha}^2M)u_{j,ji}+\mu u_{i,jj}+\bar{\alpha}Mw_{j,ji}-\beta(T_{,i}+\tau_1\dot{T}_{,i})=\rho\ddot{u}_i+\rho_f\ddot{w}_i,\quad i,j=x,y,z,\\
&\bar{\alpha}Mu_{j,ji}+Mw_{j,ji}-\frac{\beta_f}{\bar{\phi}}(T_{,i}+\tau_2\dot{T}_{,i})=\rho_f\ddot{u}_i+m\ddot{w}_i+\frac{\eta}{\bar{\kappa}}\dot{w}_i,\\
&\bar{\gamma}T_{,jj}-c(\dot{T}+\tau_3\ddot{T})-\beta T_0[(\dot{u}_{j,j}+\tau_4\ddot{u}_{j,j})+(\dot{w}_{j,j}+\tau_4\ddot{w}_{j,j})]=0,
\end{aligned}
\tag{1}
$$

where $m=\mathcal{T}\rho_f/\bar{\phi}$, the relaxation times ($\tau_1$ and τ_2) denote the temperature variation dependence of the elastic deformation, and τ_3 and τ_4 are the MVC relaxation times. The Einstein implicit summation is assumed, and a dot above a variable denotes time derivative. The Biot effective stress coefficient $\bar{\alpha}$ and coupling modulus M are (Carcione et al. 2019b)

$$
\begin{aligned}
\bar{\alpha}&=1-\frac{K_{\rm m}}{K_s},\\
M&=\frac{K_s}{1-\bar{\phi}-K_{\rm m}/K_s+\bar{\phi}K_s/K_f},\\
K_{\rm m}&=\lambda+\frac{2}{3}\mu,
\end{aligned}
\tag{2}
$$

and the thermoelasticity coefficients are related with the coefficients of thermal expansion and above coefficients. In the LS theory, $\tau_1=\tau_2=0$, $\tau_3=\tau_4$ for the classical one (Carcione et al. 2019b) and $\tau_3\neq\tau_4$ for the generalized case. The GL model holds $\tau_4=0$ and $\tau_1=\tau_2\geq\tau_3$ (Ignaczak and Ostoja-Starzewski 2010; Sharma 2018)

2.2 Plane-Wave Solution

Let us consider a Helmholtz decomposition of the two potential functions (ϕ and $\psi\hat{\mathbf{n}}$) to describe the displacement vectors $\mathbf{u}$ and $\mathbf{w}$

$$
\begin{aligned}
\mathbf{u}&=\nabla\phi_s+\nabla\times(\psi_s\hat{\mathbf{n}}),\\
\mathbf{w}&=\nabla\phi_f+\nabla\times(\psi_f\hat{\mathbf{n}}),
\end{aligned}
\tag{3}
$$

Substituting Eqs. (3) into (1), we obtain

$$
\begin{aligned}
&(\lambda+2\mu+\bar{\alpha}^2M)\nabla^2\phi_s+\bar{\alpha}M\nabla^2\phi_f-\beta(T+\tau_1\ddot{T})=\rho\ddot{\phi}_s+\rho_f\ddot{\phi}_f,\\
&\bar{\alpha}M\nabla^2\phi_s+M\nabla^2\phi_f-\frac{\beta_f}{\bar{\phi}}(T+\tau_2\dot{T})=\rho_f\ddot{\phi}_s+m\ddot{\phi}_f+\frac{\eta}{\bar{\kappa}}\dot{\phi}_f,\\
&\bar{\gamma}\nabla^2T-c(\dot{T}+\tau_3\ddot{T})-\beta T_0\nabla^2[(\dot{\phi}_s+\tau_4\ddot{\phi}_s)+(\dot{\phi}_f+\tau_4\ddot{\phi}_f)]=0,\\
&\mu\nabla^2\psi_s=\rho\ddot{\psi}_s+\rho_f\ddot{\psi}_f,\\
&\rho_f\ddot{\psi}_s+m\ddot{\psi}_f+\frac{\eta}{\bar{\kappa}}\dot{\psi}_f=0.
\end{aligned}
\tag{4}
$$

where ∇^2 is the Laplacian operator and the potential and temperature of the plane wave are

$$
\begin{aligned}
\boldsymbol{\phi}&=\mathbf{A}_{\rm P}\exp[{\rm i}(\omega t-\mathbf{k}_{\rm P}\cdot\mathbf{x})],\\
\boldsymbol{\psi}&=\mathbf{A}_{\rm S}\exp[{\rm i}(\omega t-\mathbf{k}_{\rm S}\cdot\mathbf{x})],
\end{aligned}
\tag{5}
$$

where t is the time variable, ω is the angular frequency, $\mathbf{k}_{\mathrm{P}}$ and $\mathbf{k}_{\mathrm{S}}$ are the complex wavenumber vectors for the compressional and shear waves, respectively, $\mathbf{x}$ is the position vector, $\mathrm{i}^2 = -1$ and the matrices are

$$\begin{aligned} \boldsymbol{\phi} &= \left[\phi_s,\ \phi_f,\ T\right]^{\mathrm{T}}, \quad \mathbf{A}_{\mathrm{P}} = \left[A_{\phi_s},\ A_{\phi_f},\ A_T\right]^{\mathrm{T}}, \\ \boldsymbol{\psi} &= \left[\psi_s,\ \psi_f\right]^{\mathrm{T}}, \quad \mathbf{A}_{\mathrm{S}} = \left[A_{\psi_s},\ A_{\psi_f}\right]^{\mathrm{T}}, \end{aligned} \tag{6}$$

where A_{ϕ_s}, A_{ϕ_f}, A_T, A_{ψ_s} and A_{ψ_f} are the amplitudes, and complex wavenumber is

$$\begin{aligned} &\mathbf{k} = \kappa\hat{\boldsymbol{\kappa}} - \mathrm{i}\alpha\hat{\boldsymbol{\alpha}}, \quad \mathbf{k}\cdot\mathbf{k} = k^2, \\ &\hat{\boldsymbol{\kappa}} = (\sin\theta, \cos\theta), \quad \hat{\boldsymbol{\alpha}} = (\sin(\theta-\gamma), \cos(\theta-\gamma)), \end{aligned} \tag{7}$$

where κ and α are the magnitudes of the real wavenumber and attenuation vectors, and γ and θ are the inhomogeneity and incidence angles, respectively. Thus, we get

$$\begin{aligned} &\phi = A_\phi \mathcal{E}, \quad T = A_T \mathcal{E}, \\ &\mathcal{E} = \exp\left[\mathrm{i}(\omega t - (\kappa\hat{\boldsymbol{\kappa}} - \mathrm{i}\alpha\hat{\boldsymbol{\alpha}})\cdot\mathbf{x}\right]. \end{aligned} \tag{8}$$

For homogeneous waves,

$$\gamma = 0^\circ, \quad \hat{\boldsymbol{\kappa}} = \hat{\boldsymbol{\alpha}}, \quad \mathbf{k} = k\hat{\boldsymbol{\kappa}}. \tag{9}$$

Substituting the plane waves Eqs. (8) into (4), we obtain the dispersion relation for three longitudinal waves

$$a_6 k_{\mathrm{P}}^6 + a_4 k_{\mathrm{P}}^4 + a_2 k_{\mathrm{P}}^2 + a_0 = 0, \tag{10}$$

where

$$\begin{aligned} a_6 &= \bar{\phi} E M \bar{\gamma}, \\ a_4 &= -\omega\left[\mathrm{i}\beta T_0 \bar{\tau}_4 a_{41} + \bar{\phi}(\mathrm{i}cEM\bar{\tau}_3 + \bar{\gamma}a_{42})\right], \\ a_2 &= \omega^2\left[\mathrm{i}\beta T_0 \bar{\tau}_4 a_{21} + b\bar{\phi}a_{22} + \omega^2\bar{\gamma}\bar{\phi}(m\rho - \rho_f^2) + \mathrm{i}\omega c\bar{\phi}\bar{\tau}_3 a_{23}\right], \\ a_0 &= -\mathrm{i}\omega^4\bar{\phi}c\bar{\tau}_3(\mathrm{i}b\rho + \omega m\rho - \omega\rho_f^2), \end{aligned} \tag{11}$$

and

$$\begin{aligned} &E = \lambda + 2\mu, \quad b = \frac{\eta}{\bar{\kappa}}, \quad \bar{\tau}_a = 1 - \mathrm{i}\omega\tau_a, \\ &a_{41} = M(\bar{\alpha}-1)(\bar{\alpha}\beta_f\bar{\tau}_2 - \beta\bar{\phi}\bar{\tau}_1) + \bar{\tau}_2\beta_f E, \\ &a_{42} = E(\mathrm{i}b + \omega m) + M\left[\mathrm{i}b\bar{\alpha}^2 + \omega(\bar{\alpha}^2 m - 2\bar{\alpha}\rho_f + \rho)\right], \\ &a_{21} = \omega\left[\beta\bar{\phi}\bar{\tau}_1(m - \rho_f) + \bar{\tau}_2\beta_f(\rho - \rho_f)\right], \\ &a_{22} = \mathrm{i}\bar{\gamma}\rho\omega - \beta^2 T_0\bar{\tau}_1\bar{\tau}_4 - c\bar{\tau}_3(E + M\bar{\alpha}^2), \\ &a_{23} = Em + M\bar{\alpha}^2 m + M(\rho - 2\bar{\alpha}\rho_f), \end{aligned} \tag{12}$$

Similarly, considering an S plane wave

$$\psi = A_\psi \mathcal{E}, \tag{13}$$

where A_ψ is the amplitude and replacing Eq. (13) into $(4)_4$ and $(4)_5$, we have

$$\mu(\omega m + \mathrm{i}b)k_{\mathrm{S}}^2 + \omega^3\left(\rho_f^2 - m\rho - \frac{\mathrm{i}b\rho}{\omega}\right) = 0, \tag{14}$$

so that the corresponding wavenumber is

$$k_{\mathrm{S}} = \omega\sqrt{\frac{\mathrm{i}b\rho + m\omega\rho - \omega\rho_f^2}{\mu(\mathrm{i}b + m\omega)}}. \tag{15}$$

The S wave is not affected by the thermal effects in (homogeneous) thermoelastic media.

Then, solving for κ and α, we obtain (Carcione 2014, Eq. (3.34))

$$\begin{aligned}
\kappa^2 &= \sqrt{\left[\frac{\mathrm{Re}(k^2)}{2}\right]^2 + \left[\frac{\mathrm{Im}(k^2)}{2\cos\gamma}\right]^2} + \frac{\mathrm{Re}(k^2)}{2},\\
\alpha^2 &= \sqrt{\left[\frac{\mathrm{Re}(k^2)}{2}\right]^2 + \left[\frac{\mathrm{Im}(k^2)}{2\cos\gamma}\right]^2} - \frac{\mathrm{Re}(k^2)}{2},
\end{aligned} \tag{16}$$

where wavenumber k corresponds to P-wave (k_{P}) and S-wave (k_{S}) complex wavenumbers, respectively. The expressions for the phase velocity and attenuation, assuming that the wave is inhomogeneous, are given by (Carcione 2014)

$$V_{\mathrm{ph}} = \frac{\omega}{\kappa}, \quad A = \alpha. \tag{17}$$

If the wave is homogeneous ($\gamma = 0°$), the quantities V_{ph} and A are obtained from the complex wavenumber and should be replaced by

$$V_{\mathrm{ph}} = \left[\mathrm{Re}\left(\frac{k}{\omega}\right)\right]^{-1}, \quad A = -\omega\mathrm{Im}\left(\frac{k}{\omega}\right), \tag{18}$$

and the attenuation coefficient is (Deresiewicz 1957)

$$L = 4\pi\frac{A\cdot V_{\mathrm{ph}}}{\omega}. \tag{19}$$

3 Reflection and Transmission Coefficients

We study the incidence of an inhomogeneous wave (P or S wave) striking an interface between two thermoporoelastic media as shown in Fig. 1. In the following formulation, we use superscripts I and II on the material properties to denote the incidence ($z > 0$) and transmission ($z < 0$) media. The wave incident at a certain angle generates reflected fast P (P1), thermal (T), slow Biot (P2) and shear (S) waves in the upper-medium I and four corresponding transmitted waves in the lower medium II. For clarity, the subscript 0 indicates the incident wave, and symbols 1, 2, 3 and 4 (5, 6, 7 and 8) are reflected (transmitted) P1, P2, T and S waves, respectively. Considering a planar interface in an elastic and isotropic homogeneous medium,

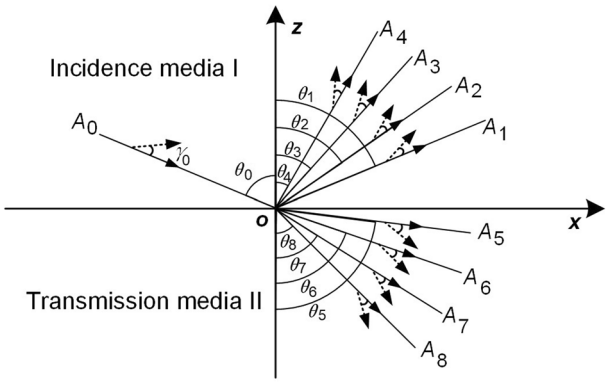

Fig. 1 Schematic plot of the inhomogeneous-waves reflection and transmission at an interface between two thermoporoelastic media. γ_0 is the inhomogeneity angle between attenuation (dashed arrows) and propagation (solid arrows) directions for incident wave

the characteristics of waves are modeled through eight boundary conditions between the two half-spaces ($z = 0$); that is (Ignaczak and Ostoja-Starzewski 2010; Wang et al. 2020a)

$$\begin{aligned} &u_z^{\mathrm{I}} = u_z^{\mathrm{II}}, \quad u_x^{\mathrm{I}} = u_x^{\mathrm{II}}, \quad \sigma_{zz}^{\mathrm{I}} = \sigma_{zz}^{\mathrm{II}}, \quad \sigma_{xz}^{\mathrm{I}} = \sigma_{xz}^{\mathrm{II}}, \\ &w_z^{\mathrm{I}} = \mathcal{Q} \cdot w_z^{\mathrm{II}}, \quad \mathcal{Q} \cdot p^{\mathrm{I}} = \mathcal{Q} \cdot p^{\mathrm{II}} + (1 - \mathcal{Q}) \cdot w_z^{\mathrm{II}}, \\ &T^{\mathrm{I}} = T^{\mathrm{II}}, \quad \bar{\kappa}^{\mathrm{I}} \frac{\partial T^{\mathrm{I}}}{\partial z} = \bar{\kappa}^{\mathrm{II}} \frac{\partial T^{\mathrm{II}}}{\partial z}, \end{aligned} \tag{20}$$

where $\mathcal{Q} = 0$ and 1 denote impermeable (pores sealed) and permeable (pores open) boundaries, respectively.

The potential functions of the plane waves are given by (similar to Hou et al. 2022b Eq. (20))

$$\begin{aligned} &\phi_s^l = \delta \Xi \phi_0^s + \sum_{a=m}^{n} \phi_a^s, \quad \phi_f^l = \delta \Xi \phi_0^f + \sum_{a=m}^{n} \phi_a^f, \\ &\psi_s^l = \delta(1 - \Xi)\psi_0^s + \psi_b^s, \quad \psi_f^l = \delta(1 - \Xi)\psi_0^f + \psi_b^f, \end{aligned} \tag{21}$$

where if $\Xi = 1$ corresponds to an incident P wave and if $\Xi = 0$ is S mode. For incidence (reflection) media (l denotes I and $\delta = 1$), $m = 1$, $n = 3$ and $b = 4$, whereas for transmission case (l denotes II) that $m = 5$, $n = 7$, $b = 8$ and $\delta = 0$. And displacement potentials are

$$\begin{aligned} &\phi_a = A_a \exp[\mathrm{i}(\omega t - \mathbf{k}_a \cdot \mathbf{x})], \quad a = 0,\ 1,\ ...,\ 7 \text{ and} \neq 4, \\ &\psi_b = A_b \exp[\mathrm{i}(\omega t - \mathbf{k}_b \cdot \mathbf{x})], \quad b = 4,\ 8, \end{aligned} \tag{22}$$

where A_a and A_b are the amplitudes and the wave vectors are

$$\mathbf{k}_c \cdot \mathbf{x} = p_c x + q_c z, \quad c = 0, 1, \ldots 8, \tag{23}$$

the horizontal wavenumber p_c remains unchanged during the propagation following the generalized Snell law (Carcione 2014; Borcherdt 2009) and the vertical wavenumbers q_c obtained from complex wavenumbers k_c

$$\begin{aligned} &p_c = |\kappa| \sin\theta + \mathrm{i}|\alpha| \sin(\theta - \gamma), \\ &q_c = D_R + \mathrm{i}D_I, \quad D = \pm \mathrm{pv}\sqrt{k_c^2 - p_c^2}, \end{aligned} \tag{24}$$

where $\mathrm{pv}\sqrt{W}$ denotes the principal value of the square root of the complex number W. The downward waves correspond to the minus signs otherwise are positive to ensure the decay of the reflected and transmitted waves along the positive z-direction.

Combining the boundary conditions Eq. (20) with potentials (3) and (21), we obtain the matrix form

$$\sum_{b=1}^{8} \left(G_{ab} \cdot X_b\right) = Y_a, \quad a = 1,\ 2,\ ...,\ 8. \tag{25}$$

The column vector $\mathbf{X}$ consists of the complex-valued amplitude ratios, defined as

$$X_b = \frac{A_b^s}{A_0^s}, \tag{26}$$

and the explicit expressions of $\mathbf{G}$ and $\mathbf{Y}$ in Eq. (25) are

$$\begin{cases}
G_{1a} = q_a, \quad G_{2a} = p_a, \\
G_{3a} = (p_a^2 + q_a^2)(-M^{\mathrm{I}}(\alpha^{\mathrm{I}})^2 - M^{\mathrm{I}}\alpha^{\mathrm{I}}\mathcal{V}_a - \lambda^{\mathrm{I}}) + \delta_a\beta^{\mathrm{I}}(\mathrm{i}\omega\tau_1^{\mathrm{I}} - 1) - 2\mu^{\mathrm{I}}q_a^2, \quad G_{4a} = 2\mu^{\mathrm{I}}p_a q_a, \\
G_{5a} = q_a\mathcal{V}_a, \quad G_{6a} = \mathcal{Q}\left((p_a^2 + q_a^2)M^{\mathrm{I}}(\mathcal{V}_a + \alpha^{\mathrm{I}}) - \dfrac{\delta_a\beta_f^{\mathrm{I}}}{\phi^{\mathrm{I}}}(\mathrm{i}\omega\tau_2^{\mathrm{I}} - 1)\right), \\
G_{7a} = \delta_a, \quad G_{8a} = \bar{\gamma}^{\mathrm{I}}\delta_a q_a, \quad (a = 1, 2, 3), \\
G_{1b} = q_b, \quad G_{2b} = -p_b, \\
G_{3b} = (p_b^2 + q_b^2)(M^{\mathrm{II}}(\alpha^{\mathrm{II}})^2 + M^{\mathrm{II}}\alpha^{\mathrm{II}}\mathcal{V}_b + \lambda^{\mathrm{II}}) - \delta_b\beta^{\mathrm{II}}(\mathrm{i}\omega\tau_1^{\mathrm{II}} - 1) + 2\mu^{\mathrm{II}}q_b^2, \quad G_{4b} = 2\mu^{\mathrm{II}}p_b q_b, \\
G_{5b} = \mathcal{Q}q_b\mathcal{V}_b, \quad G_{6b} = \mathcal{Q}\left(-(p_b^2 + q_b^2)M^{\mathrm{II}}(\mathcal{V}_b + \alpha^{\mathrm{II}}) + \dfrac{\delta_b\beta_f^{\mathrm{II}}}{\phi^{\mathrm{II}}}(\mathrm{i}\omega\tau_2^{\mathrm{II}} - 1)\right) + (1 - \mathcal{Q})G_{5b}, \\
G_{7b} = -\delta_b, \quad G_{8b} = \bar{\gamma}^{\mathrm{II}}\delta_b q_b, \quad (b = 5, 6, 7), \\
G_{14} = p_4, \quad G_{18} = -p_8, \\
G_{24} = -q_4, \quad G_{28} = -q_8, \\
G_{34} = -2\mu^{\mathrm{I}}p_4 q_4, \quad G_{38} = -2\mu^{\mathrm{II}}p_8 q_8, \\
G_{44} = \mu^{\mathrm{I}}(p_4^2 - q_4^2), \quad G_{48} = -\mu^{\mathrm{II}}(p_8^2 - q_8^2), \\
G_{54} = \phi^{\mathrm{I}}p_4(\mathcal{V}_4 - 1), \quad G_{58} = -\phi^{\mathrm{II}}p_8(\mathcal{V}_8 - 1), \\
G_{68} = (1 - \mathcal{Q})G_{58}, \quad G_{64} = G_{74} = G_{78} = G_{84} = G_{88} = 0,
\end{cases} \tag{27}$$

and

$$\begin{cases}
Y_1 = \Xi q_0 - (1 - \Xi)p_0, \quad Y_2 = -\Xi p_0 - (1 - \Xi)q_0, \\
Y_3 = \Xi\left((p_0^2 + q_0^2)(M^{\mathrm{I}}(\alpha^{\mathrm{I}})^2 + M^{\mathrm{I}}\alpha^{\mathrm{I}}\mathcal{V}_0 + \lambda) - \delta_0\beta^{\mathrm{I}}(\mathrm{i}\omega\tau_1^{\mathrm{I}} - 1) + 2\mu^{\mathrm{I}}q_0^2\right) - 2\mu^{\mathrm{I}}p_0 q_0(1 - \Xi), \\
Y_4 = 2\mu^{\mathrm{I}}p_0 q_0\Xi - \mu^{\mathrm{I}}(p_0^2 - q_0^2)(1 - \Xi), \\
Y_5 = \Xi q_0\mathcal{V}_0 - p_0\mathcal{V}_0(1 - \Xi), \\
Y_6 = \Xi\left(-(p_0^2 + q_0^2)M^{\mathrm{I}}(\mathcal{V}_0 + \alpha^{\mathrm{I}}) + \dfrac{\delta_0\beta_f^{\mathrm{I}}}{\phi^{\mathrm{I}}}(\mathrm{i}\omega\tau_2^{\mathrm{I}} - 1)\right), \\
Y_7 = -\Xi\delta_0, \quad Y_8 = \bar{\gamma}^{\mathrm{I}}\delta_0 q_0\Xi,
\end{cases} \tag{28}$$

and

$$\begin{aligned}
\mathcal{V}_a &= \frac{\beta\bar{\phi}\bar{\tau}_1\left(M\bar{\alpha}(p_0^2+q_0^2)-\omega^2\rho_f\right)-\bar{\tau}_2\beta_f\left((E+\bar{\alpha}^2M)(p_0^2+q_0^2)-\rho\omega^2\right)}{\beta\bar{\phi}\bar{\tau}_1\left(m\omega^2+\mathrm{i}b\omega-M(p_0^2+q_0^2)\right)+\bar{\tau}_2\beta_f\left(M\bar{\alpha}(p_0^2+q_0^2)-\rho_f\omega^2\right)},\\
\delta_a &= \frac{\mathrm{i}\omega\beta\bar{\tau}_4T_0(1+\mathcal{V}_a)(p_0^2+q_0^2)}{\mathrm{i}\omega\bar{\tau}_2c-\bar{\gamma}(p_0^2+q_0^2)}, \quad a=0,\ 1,\ ...,\ 7 \text{ and } \neq 4,\\
\mathcal{V}_b &= \frac{-\omega\rho_f}{m\omega+\mathrm{i}\eta/\bar{\kappa}}, \quad b=4,\ 8,
\end{aligned} \tag{29}$$

where $a = 0,\ 1,\ 2,\ 3$ and $b = 4$ correspond to medium I parameters (with superscript I), while 5 to 8 are medium II (with superscript II).

Once the linear system is solved, the reflection (R_a) and transmission (T_b) coefficients are calculated using complex wavenumbers k_a (or k_b)

$$\begin{aligned}
R_a &= \frac{A_a}{A_0}\frac{k_a}{k_0} = \left|R_a\right|\exp(\mathrm{i}\vartheta_a), \quad a=1,2,3,4,\\
T_b &= \frac{A_b}{A_0}\frac{k_b}{k_0} = \left|T_b\right|\exp(\mathrm{i}\vartheta_b), \quad b=5,6,7,8,
\end{aligned} \tag{30}$$

where $\left|R_a\right|$ and $\left|T_b\right|$ denote the R/T amplitudes, while ϑ_a and ϑ_b are the corresponding phase angles.

4 Energy Partitions

Wang et al. (2020a) give the energy flux for double-porosity theory, and the corresponding energy balance is given. Here, the time-averaged energy flow along the z-direction $\left\langle \mathcal{F}_z \right\rangle$ holding for the thermoporoelastic case is developed (Sharma 2018) by

$$\left\langle \mathcal{F}_z \right\rangle = \frac{1}{2}\mathrm{Re}\left(\sigma_{zz}\dot{u}_z^* + \sigma_{xz}\dot{u}_x^* - p\dot{w}_z^*\right). \tag{31}$$

The energy partitions are denoted by

$$\left\langle \mathcal{F}_{ab}^{\mathrm{i}} \right\rangle = \frac{1}{2}\mathrm{Re}\left(\sigma_{zz}^a(\dot{u}_z^*)^b + \sigma_{xz}^a(\dot{u}_x^*)^b - p^a(\dot{w}_z^*)^b\right), \tag{32}$$

where $a,\ b = 0,\ 1, \cdots, 4$ denote the incidence $\left(\left\langle \mathcal{F}_{ab}^{\mathrm{i}} \right\rangle\right)$, $a,\ b = 5,\ 6,\ 7,\ 8$ are transmission $\left(\left\langle \mathcal{F}_{ab}^{\mathrm{t}} \right\rangle\right)$ medium, the star denotes the complex conjugate, and the indices a and b of stresses and displacements correspond to the different waves (same as Eq. 30).

The procedure to obtain the energy balance based on the energy ratios is

$$\sum_{a=1}^{4}\sum_{b=1}^{4}\left\langle \mathcal{F}_{ab}^{\mathrm{i}} \right\rangle + \sum_{a=1}^{4}\left(\left\langle \mathcal{F}_{0a}^{\mathrm{i}} \right\rangle + \left\langle \mathcal{F}_{a0}^{\mathrm{i}} \right\rangle\right) - \sum_{a=5}^{8}\sum_{b=5}^{8}\left\langle \mathcal{F}_{ab}^{\mathrm{t}} \right\rangle = -\left\langle \mathcal{F}_{00}^{\mathrm{i}} \right\rangle. \tag{33}$$

The R/T coefficients (Eq. (30)) are verified by energy conservation, which is calculated by the energy ratios (see Hou et al. (2022b), Eqs. (47) and (48)). Let diagonal entries E_{aa}^{i} and E_{bb}^{t} represent the energy ratios of reflected and transmitted waves, and off-diagonal E_{ab}^{i} and E_{ab}^{t} represent the corresponding interference energy ratios, which are

Table 1 Medium properties

Grain bulk modulus, $K_s^{\mathrm{I}}/K_s^{\mathrm{II}}$	35/35 GPa
Density, $\rho_s^{\mathrm{I}}/\rho_s^{\mathrm{II}}$	2650/2650 kg/m^3
Frame bulk modulus, $K_m^{\mathrm{I}}/K_m^{\mathrm{II}}$	1.7/1.7 GPa
Shear modulus, $\mu^{\mathrm{I}}/\mu^{\mathrm{II}}$	1.885/1.885 GPa
Porosity, $\bar{\phi}^{\mathrm{I}}/\bar{\phi}^{\mathrm{II}}$	0.3/0.3
Permeability, $\bar{\kappa}^{\mathrm{I}}/\bar{\kappa}^{\mathrm{II}}$	1/1 Darcy
Tortuosity, $\mathcal{T}^{\mathrm{I}}/\mathcal{T}^{\mathrm{II}}$	2/2
Fluid density, $\rho_f^{\mathrm{I}}/\rho_f^{\mathrm{II}}$	700/1000 kg/m^3
Viscosity, $\eta_f^{\mathrm{I}}/\eta_f^{\mathrm{II}}$	0.004/0.001 Pa s
Bulk modulus, $K_f^{\mathrm{I}}/K_f^{\mathrm{II}}$	0.6/2.4 GPa
Thermoelasticity coefficient, $\beta_f^{\mathrm{I}}/\beta_f^{\mathrm{II}}$	$8\times10^5/8\times10^5$ kg/(m·s^2·K)
Bulk specific heat, $c^{\mathrm{I}}/c^{\mathrm{II}}$	$1.8\times10^6/3.2\times10^6$ kg/(m·s^2·K)
Thermoelasticity coefficient, $\beta^{\mathrm{I}}/\beta^{\mathrm{II}}$	$2.5\times10^6/2.5\times10^6$ kg/(m·s^2·K)
Absolute temperature, $T_0^{\mathrm{I}}/T_0^{\mathrm{II}}$	300/300 K
Thermal conductivity, $\bar{\gamma}^{\mathrm{I}}/\bar{\gamma}^{\mathrm{II}}$	4.5/8.7 m·kg/(s^3·K)
Relaxation time, τ_1^{I} (τ_2^{I})/τ_1^{II} (τ_2^{II})	0.3/0.3 ns
' ', τ_3^{I} (τ_4^{I})/τ_3^{II} (τ_4^{II})	0.15/0.15 ns

$$
\begin{aligned}
E_{aa}^{\mathrm{i}} &= \sum_{a=1}^{4} \frac{\langle \mathcal{F}_{aa}^{\mathrm{i}} \rangle}{\langle \mathcal{F}_{00}^{\mathrm{i}} \rangle}, \quad E_{ab}^{\mathrm{i}} = \sum_{a=0}^{4} \left(\sum_{b=0}^{4} \frac{\langle \mathcal{F}_{ab}^{\mathrm{i}} \rangle}{\langle \mathcal{F}_{00}^{\mathrm{i}} \rangle} - E_{aa}^{\mathrm{i}} \right), \\
E_{aa}^{\mathrm{t}} &= \sum_{a=5}^{8} \frac{\langle \mathcal{F}_{aa}^{\mathrm{t}} \rangle}{\langle \mathcal{F}_{00}^{\mathrm{i}} \rangle}, \quad E_{ab}^{\mathrm{t}} = \sum_{a=5}^{8} \left(\sum_{b=5}^{8} \frac{\langle \mathcal{F}_{ab}^{\mathrm{t}} \rangle}{\langle \mathcal{F}_{00}^{\mathrm{i}} \rangle} - E_{aa}^{\mathrm{t}} \right), \\
E_{\mathrm{cons}} &= \sum_{a=1}^{4} \sum_{b=1}^{4} \frac{\langle \mathcal{F}_{ab}^{\mathrm{i}} \rangle}{\langle \mathcal{F}_{00}^{\mathrm{i}} \rangle} + \sum_{a=1}^{4} \left(\frac{\langle \mathcal{F}_{0a}^{\mathrm{i}} \rangle}{\langle \mathcal{F}_{00}^{\mathrm{i}} \rangle} + \frac{\langle \mathcal{F}_{a0}^{\mathrm{i}} \rangle}{\langle \mathcal{F}_{00}^{\mathrm{i}} \rangle} \right) - \sum_{a=5}^{8} \sum_{b=5}^{8} \frac{\langle \mathcal{F}_{ab}^{\mathrm{t}} \rangle}{\langle \mathcal{F}_{00}^{\mathrm{i}} \rangle} = -1.
\end{aligned}
\tag{34}
$$

5 Examples

Oil–water contacts are commonly encountered in the transition zone of hydrocarbon reservoirs. We evaluate the influence of thermoelastic parameters on the *R*/*T* characteristics (amplitudes, phase angles and energies) of inhomogeneous plane waves at an oil–water interface. The properties of the medium used in the following numerical simulations are listed in Table 1, which are used and validated by Corredor et al. (2014) and Wang et al. (2021).

We assume that the porous medium background is an unconsolidated sandstone with a porosity of 30%. On the basis of the properties of Table 1, Figs. 2 and 3 display the phase velocity and attenuation coefficient as a function of frequency for the oil-saturated (Incidence I) and water-saturated (Transmission II) cases, respectively. The results are obtained based on the thermoporoelastic LS and GL theories, respectively. We see that the fast P (P1) wave has two Zener-like relaxation peaks, related to the

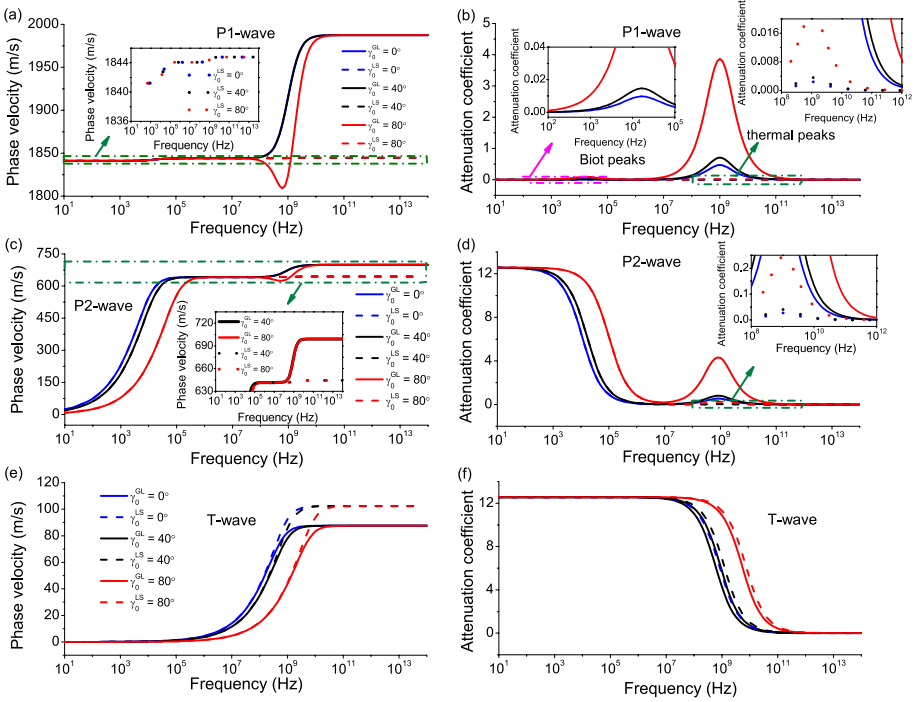

Fig. 2 Phase velocities (**a**, **c**, **e**) and attenuation coefficients (**b**, **d**, **f**) of the P1, P2 and T waves as a function of frequency at oil-saturated media (incidence media I). The blue, black and red lines correspond to the results of the $\gamma_0 = 0°$, 40° and 80°, and solid and dashed lines are for the GL and LS theories

Biot (approximately 10 kHz) and thermal (approximately 1 GHz) loss mechanisms. The former induces the velocity dispersion of the P1 and P2 waves. The associated thermal attenuation only affects wave propagation at high frequencies, especially for the T wave. For clarity, we enlarge the phase velocities and attenuations of P1 and P2 waves at relaxation peaks as shown in Figs. 2a–2d and 3a–3d).

The GL model predicts more pronounced velocity dispersions and higher thermal attenuations of P1 and P2 waves than the LS model. The P2 and T waves are strongly diffusive at low frequencies and more wave-like at the high range. Due to the influence of relaxation times, the GL shows a higher P2-wave velocity than that of the LS model, whereas the behavior of the T wave is the opposite. The *R*/*T* properties depend on inhomogeneity angles. The inhomogeneous waves (P1 and P2) show higher velocity dispersion and stronger attenuation than the homogeneous waves, especially for the inhomogeneity angle closer to 90°. The water-saturated medium has a higher velocity than the oil-saturated medium as expected. In the following, we consider an incident wave with a frequency of 1 GHz (corresponding to the thermal relaxation peak) to highlight the thermal effect as well as the difference between the LS and GL models.

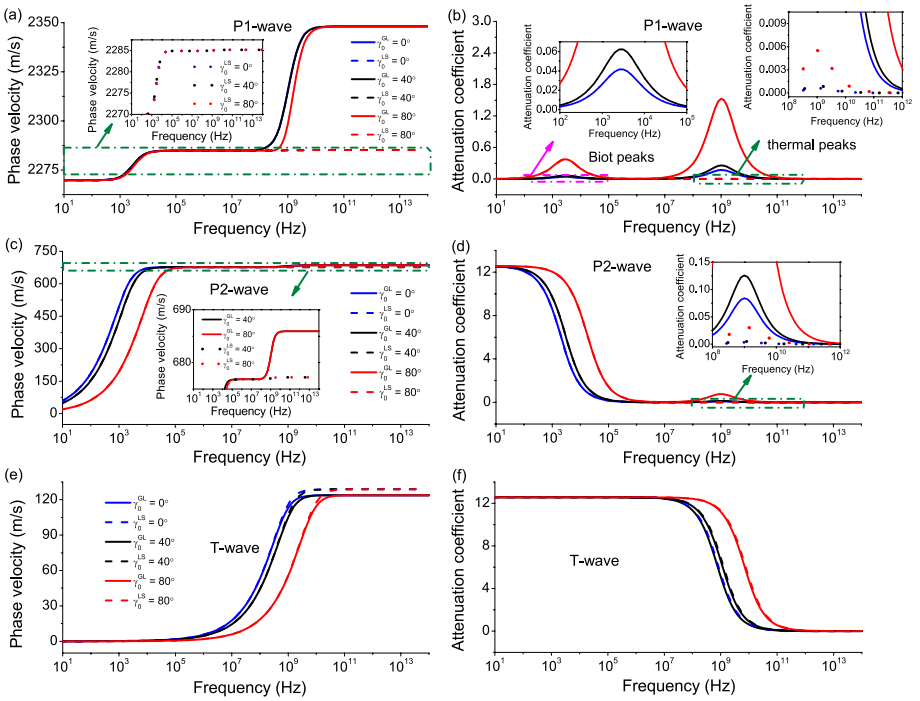

Fig. 3 Same as Fig. 2 but for the water-saturated media (transmission media II)

5.1 P-Wave Incidence

The results for the LS and GL models with P-wave incidence are plotted as the solid and dashed lines in Figs. 4, 5, 6, 7, respectively. In Figs. 4 and 6, we see that both models have similar S-wave *R*/*T* coefficients and energies at small angles of incidence. But become differentiated near the P-wave critical angle due to the velocity variation of velocities (see Figs. 2 and 3). Under the same condition (homogeneous or inhomogeneous), the LS model predicts higher amplitudes of the *R*/*T* P2 waves than the GL model, which becomes the opposite for the reflected T wave. As shown in Figs. 4d, h, 6d, h, the S-wave amplitudes and energy fluxes vanish at normal incidence because there is no converted wave. However, the *R*/*T* S waves by the GL model show half-phase effects due to inhomogeneity angles (see Fig. 5d, h). The overall discrepancy in the *R*/*T* phases is small.

Figure 6 shows the partition of energy, where the transmitted P1-wave energy decreases with increasing angles. For incidences beyond 50°, the energy in the vertical direction by the LS model vanishes until grazing incidence, because the wave propagates along the interface, carrying no energy flux in the vertical direction. Since the theory predicts a very low attenuation (see Figs. 2b and 3b), the medium behaves elastically at a frequency of 1 GHz. The opposite behavior is observed for the reflected P1 wave, where the energy increases gradually with increasing angles. The influence of inhomogeneity angles on the *R*/*T* waves is particularly evident near grazing incidence (see Fig. 6b–h), where the effect on the reflected P is maximum at the critical angle. The GL model predicts more interference energy (see Fig. 7b) due to its sensitivity to thermal attenuation than the LS model.

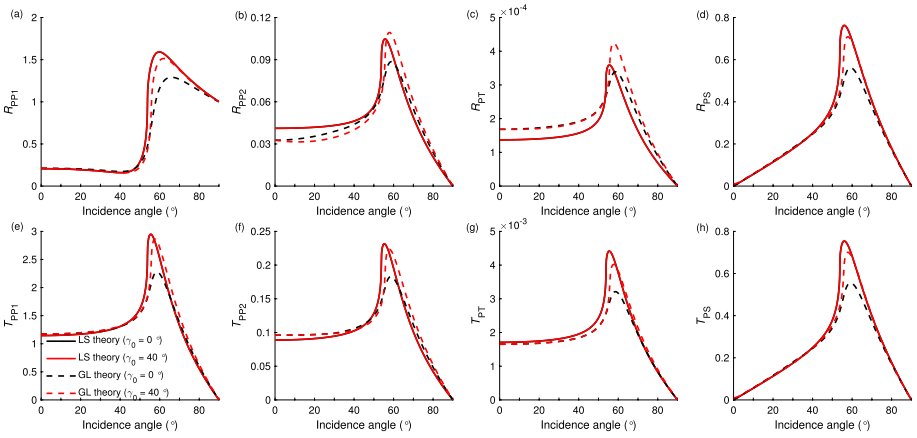

Fig. 4 Reflection and transmission amplitudes as a function of the P-wave incidence angle, corresponding to the LS (solid lines) and GL (dashed lines) models at 1 GHz for homogeneous $\gamma_0 = 0°$ and inhomogeneous $\gamma_0 = 40°$ cases

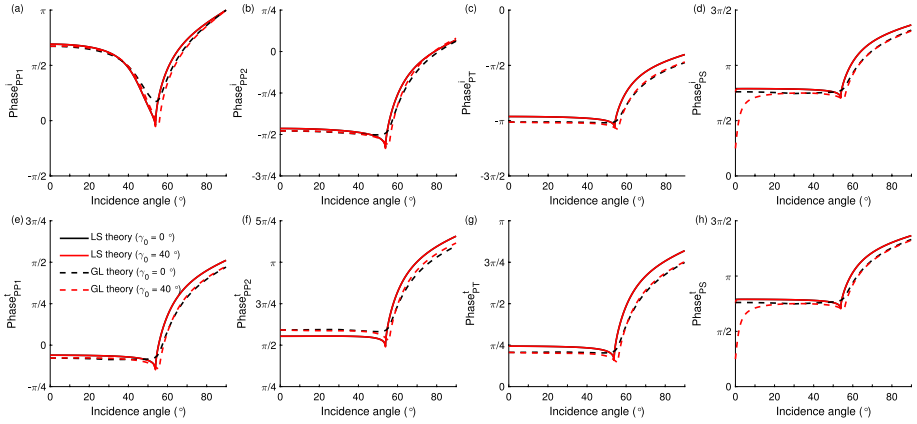

Fig. 5 Same as Fig. 4 but for the phase angles

The energy conservation at the interface is guaranteed as the sum of all the ratios is -1 (see Fig. 7a).

5.2 S-Wave Incidence

Figures 8, 9, 10 show the *R*/*T* coefficients, phases, and energy ratios as a function of incidence angles for different inhomogeneity angles, respectively. Since the S-wave wavenumber is real, the inhomogeneity angle has no effect as can be seen in Figs. 8, 9, 10, 11 where both the homogeneous ($\gamma_0 = 0°$) and inhomogeneous ($\gamma_0 = 40°$) waves produce the same results for the LS (black and red solid lines, respectively) and GL (black and red dashed lines, respectively) models, respectively, in the whole range

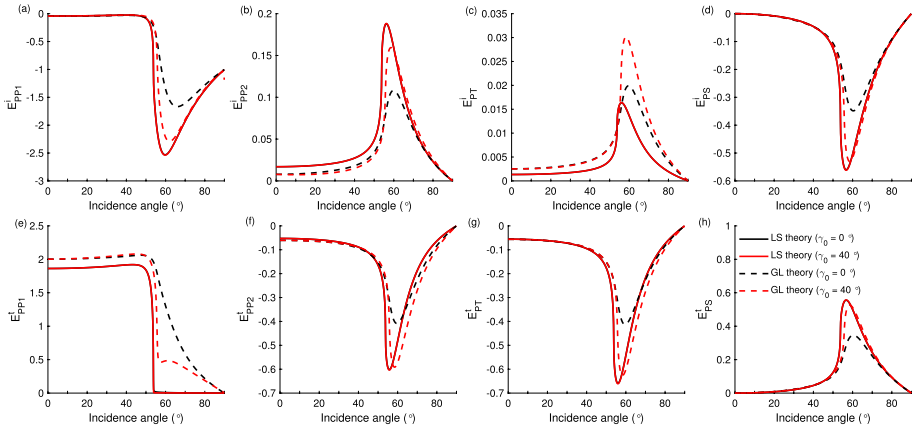

Fig. 6 Same as Fig. 4 but for the energy ratios, considering the flux in the z-direction

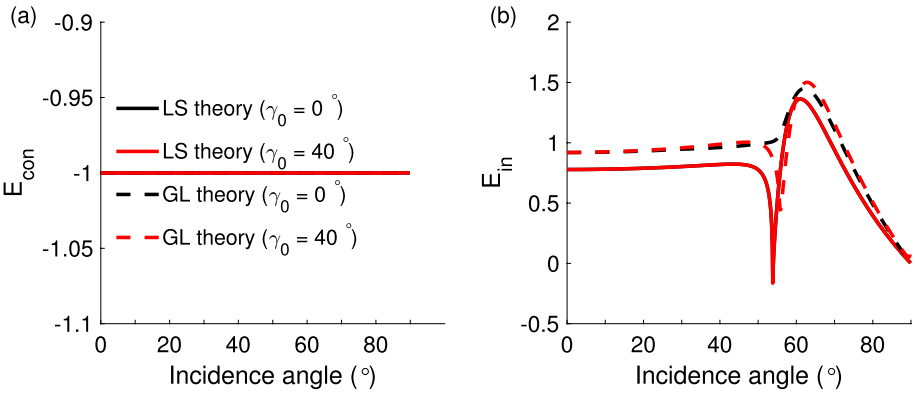

Fig. 7 Same as Fig. 4 but for the sum of the energy ratios (energy balance) (**a**) and the interference energy (**b**)

of incidence angles. As shown in Fig. 8, the solutions by the two theories show similar angle-dependent features for these *R*/*T* P1, P2, and T waves, with the increasing difference occurring after the critical angle. whereas the *R*/*T* S-wave results of the two theories coincide. Intriguingly, such discrepancies become negligible when the angle nears grazing incidence. Since the velocity of the incident S wave is lower than the *R*/*T* P1 velocities, there exist two peaks of longitudinal waves. The LS solution predicts wave amplitudes higher at the first peak but lower around the second peak than the GL solution. This shows a complex coupled mode with the thermal effect. For the *R*/*T* S waves, the two theories produce the same solutions.

Figure 9 shows that both theories have consistent trends in phase angle. In Fig. 10, the behavior of P-wave energies by the LS theory is analogous to that of the P-wave incidence (see Fig. 6) due to the elastic characteristic of low attenuation shown in Figs. 10a, e. As expected, the energies and amplitudes of the P2, T, and S waves have similar variations. Moreover, the GL model predicts more interference energy than the LS one, as shown in Fig. 11b. The energy conservation at the interface is satisfied as exhibited in Fig. 11a.

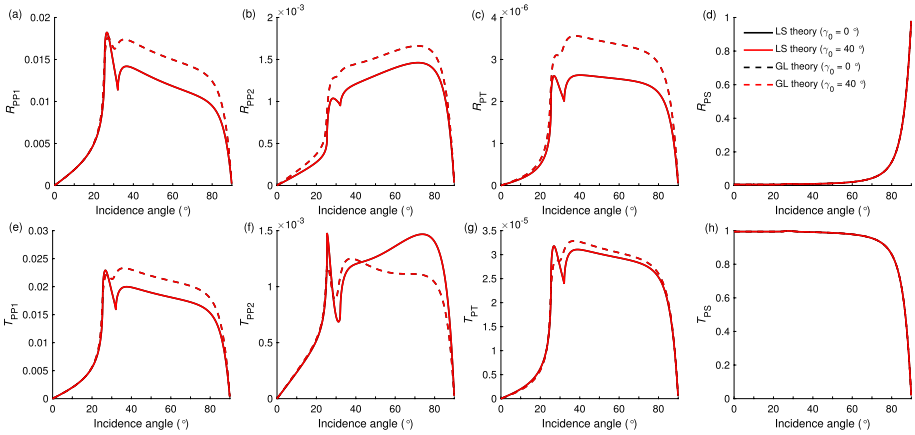

Fig. 8 Reflection and transmission amplitudes as a function of the S-wave incidence angle, corresponding to the LS (solid lines) and GL (dashed lines) models at 1 GHz for homogeneous $\gamma_0 = 0°$ and inhomogeneous $\gamma_0 = 40°$ cases

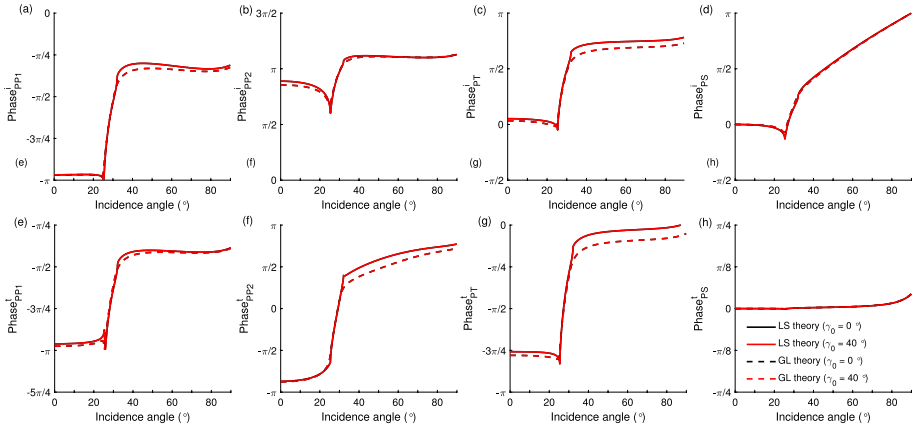

Fig. 9 Same as Fig. 8 but for the phase angles

5.3 Generalized LS Theory

Let us consider the generalized LS model by assuming different values of relaxation time τ_4 (Wang et al. 2021)

$$\tau_4^{\mathrm{I}} = \tau_4^{\mathrm{II}} = 0.15 \text{ ns},\ 0.30 \text{ ns},\ 0.45 \text{ ns}. \tag{35}$$

We compare different thermoporoelastic models with the classical Biot poroelastic theory to highlight the influence of thermal characteristics. Figures 12 and 13 show the phase velocity and attenuation as a function of frequency for different models with $\gamma_0 = 40°$. We see that the Biot theory predicts lower velocities of the P1 and P2 waves at all the frequencies and weaker Biot dispersion for the P1 wave, implying strong thermal effects on wave

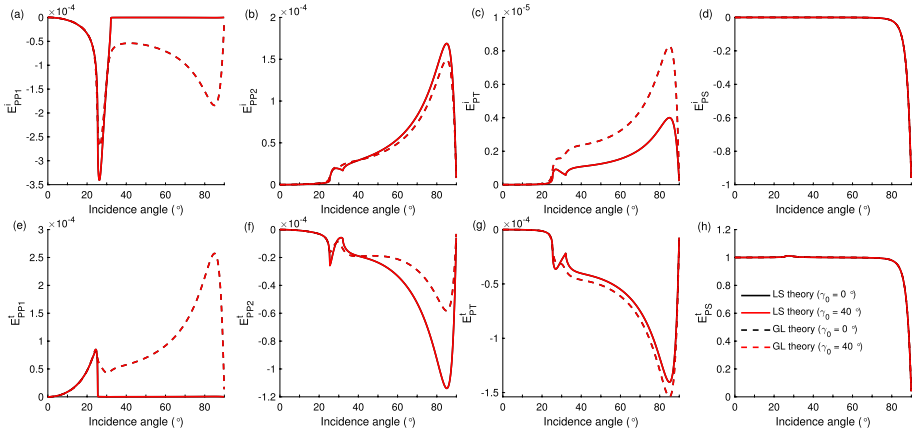

Fig. 10 Same as Fig. 8 but for the energy ratios, considering the flux in the z-direction

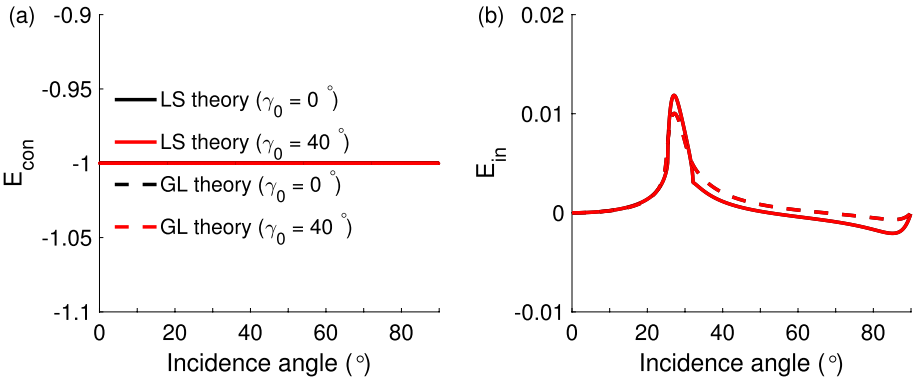

Fig. 11 Same as Fig. 8 but for the sum of the energy ratios (energy balance) (**a**) and the interference energy (**b**)

propagation. With increasing τ_4, the P1 wave presents increasing thermal attenuation and velocity dispersion, while the relaxation frequency remains unchanged. The thermal effect on the P2 wave is similar to the P1 wave at high frequencies, but is contrary to the T wave. Note that, for the case $\tau_4 = \tau_1 = \tau_2 = 0.30$ ns, the LS prediction agrees with the result by the GL model (Ignaczak and Ostoja-Starzewski 2010; Wang et al. 2021), implying that varying τ_4 can determine different levels of dispersion.

Next, we focus on the analysis of the P1-wave incidence, which is of primary interest in exploration applications. We use the parameters based on Figs. 12 and 13 at 1 GHz. Figure 14 shows the R/T coefficients as a function of incidence angles with $\gamma_0 = 40°$. The results associated with different models show an evident dependence on thermal characteristics. The Biot model predicts a smaller critical angle because of ignoring the thermal parameters. The Biot model displays stronger magnitudes for the P2 waves than the LS and GL cases, whereas the opposite behavior occurs for the P1 and converted S waves due to the existence of the T waves. The GL theory shows an analogous behavior to the generalized LS model at $\tau_4 = 0.30$ ns as shown in Fig. 14. Irrespective if the interface is open (see

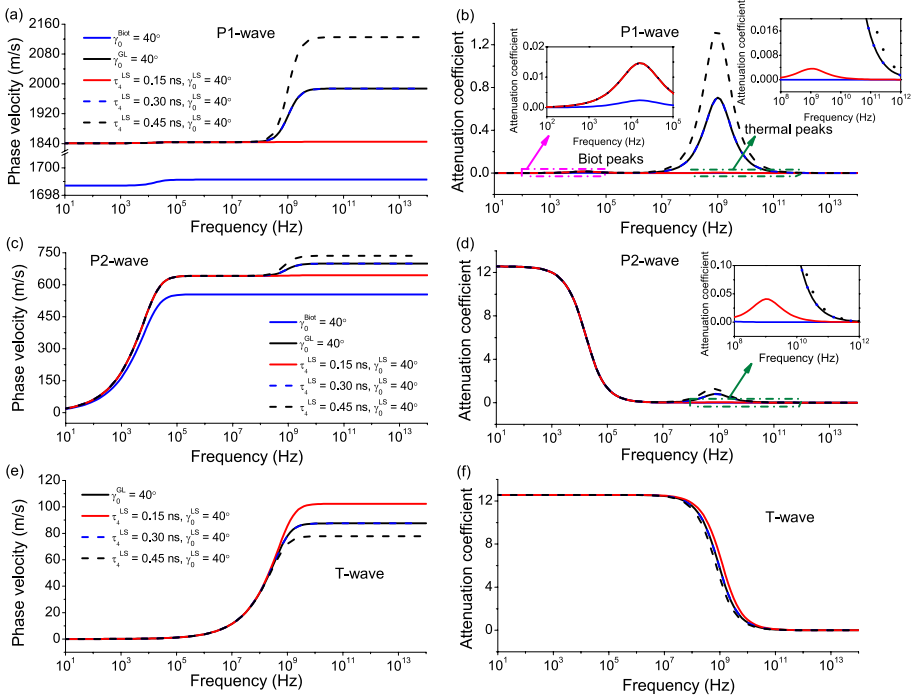

Fig. 12 Phase velocities (**a**, **c**, **e**) and attenuation coefficients (**b**, **d**, **f**) of the P1, P2 and T waves as a function of frequency at incidence media I (1 GHz). The blue, black and red solid lines correspond to the results of the classical Biot, GL and LS models with $\gamma_0 = 40°$, whereas blue and black dashed lines to the generalized LS theory with $\tau_4 = 0.30$ ns and $\tau_4 = 0.45$ ns, respectively

Fig. 14) or sealed (see Fig. 15), increasing τ_4 decreases the amplitude of the reflected P wave at small incidence angles, but will be the opposite at large ones. The dependence of P2 and S waves on the boundary conditions can be seen in the coefficients and energies shown in Figs. 14 and 15, where we have assumed a sealed boundary.

6 Conclusions

We describe the *R*/*T* phenomenon of inhomogeneous plane waves at an interface between two dissimilar fluid-saturated thermoporoelastic media, where the theory is formulated in terms of the classic LS, generalized LS and GL models, respectively. The presence of thermal characteristics with relaxation times makes the media behave anelastically, which means that the propagation and attenuation directions do not necessarily coincide. The propagation characteristics (Biot and thermal peaks) of inhomogeneous waves significantly depend on the inhomogeneity angle in the dispersion range, with a lower phase velocity and stronger thermal attenuation than those of homogeneous waves. Considering the oil–water contact, we investigate the effects of types of incident wave, incidence and inhomogeneity angles, relaxation times, and boundary conditions on the *R*/*T* coefficients and associated phase angles and energy ratios. For an incident P wave, the effect of inhomogeneity angles on the energy partition becomes noticeable at the critical angle, whereas S-wave incidence is independent of inhomogeneity

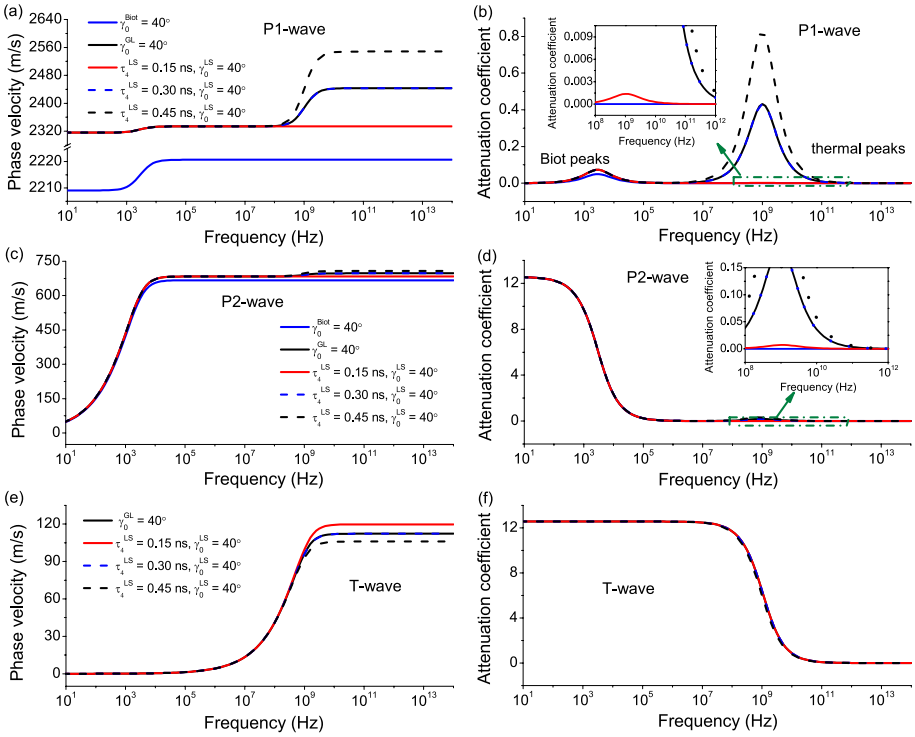

Fig. 13 Same as Fig. 12 but for the transmission media II

angles. We compare these thermoporoelastic models (LS, GL, and generalized LS) with the classical Biot poroelastic theory. The results show that the angle-dependent thermoporoelastic attenuation couples both the effects of thermoelasticity and poroelasticity. The relaxation time affects the P1-wave velocity dispersion more than other waves, whereas the P2 and S waves mainly depend on boundary conditions. The classical Biot model predicts lower velocities of the P1 and P2 waves, but shows stronger magnitudes for the P2 waves. Considering the influence of thermal parameters on *R*/*T* inhomogeneous waves, more accurate reservoir information can be obtained, which provides theoretical support for seismic exploration.

Appendix A

The constitutive relations for the stress σ_{ij}, strain ϵ_{ij} and fluid pressure p of thermoporoelasticity can be expressed as follows (Wang et al. 2021):

$$\begin{aligned} \sigma_{ij} &= 2\mu\epsilon_{ij} + [\lambda\epsilon_m + \bar{\alpha}M\epsilon - \beta(T + \tau_1\dot{T})]\delta_{ij}, \\ -p &= M\epsilon - \frac{\beta_f}{\bar{\phi}}(T + \tau_2\dot{T}), \\ \epsilon &= \bar{\alpha}\epsilon_m + \epsilon_f, \quad \epsilon_m = u_{i,i}, \quad \epsilon_f = w_{i,i}, \quad 2\epsilon_{ij} = u_{i,j} + u_{j,i}, \end{aligned} \tag{A.1}$$

where δ_{ij} is the Kronecker function. The equations of momentum conservation are

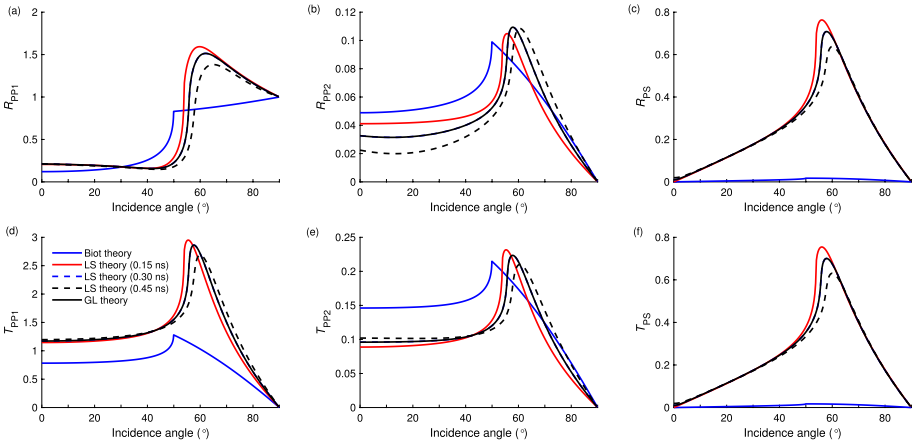

Fig. 14 Reflection and transmission amplitudes as a function of the P-wave incidence angle, corresponding to the classical Biot (blue solid lines), GL (black solid lines) and LS (red solid lines) models with $\gamma_0 = 40°$, whereas blue and black dashed lines to the generalized LS theory with $\tau_4 = 0.30$ ns and $\tau_4 = 0.45$ ns, respectively

$$\begin{aligned} \sigma_{ij,j} &= \rho\ddot{u}_i + \rho_f\ddot{w}_i, \\ -p_{,i} &= \rho_f\ddot{u}_i + m\ddot{w}_i + \frac{\eta}{\bar{\kappa}}\dot{w}_i. \end{aligned} \tag{A.2}$$

Substituting the stress–strain relation (Eq. (A.1)) into the equations of momentum conservation (Eq. (A.2)) and strain–displacement relations, we obtain compact equations for displacement components

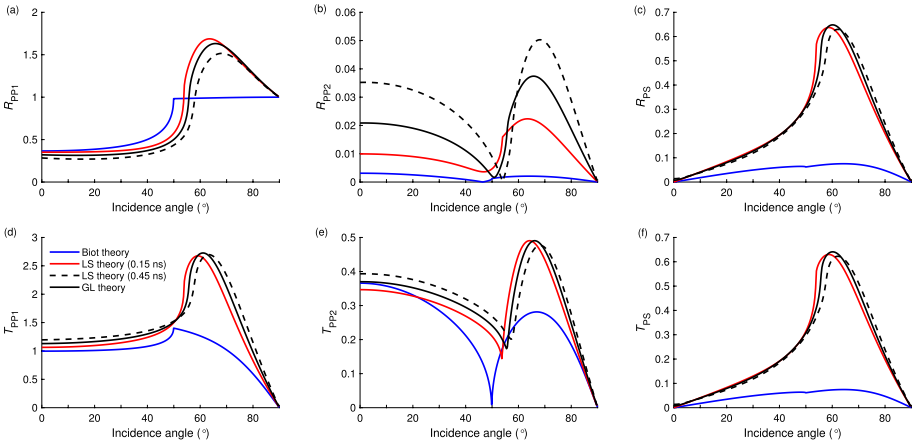

Fig. 15 Reflection and transmission amplitudes as a function of the P-wave incidence angle, corresponding to the classical Biot (blue solid lines), GL (black solid lines) and LS (black dashed $\tau_4 = 0.15$ ns and black solid $\tau_4 = 0.45$ ns lines) models with $\gamma_0 = 40°$, whereas the boundary is sealed

$$
\begin{aligned}
&(\lambda+\mu+\bar{\alpha}^2 M)u_{j,ji}+\mu u_{i,jj}+\bar{\alpha}Mw_{j,ji}-\beta(T_{,i}+\tau_1\dot{T}_{,i})=\rho\ddot{u}_i+\rho_f\ddot{w}_i, \quad i,j=x,y,z,\\
&\bar{\alpha}Mu_{j,ji}+Mw_{j,ji}-\frac{\beta_f}{\bar{\phi}}(T_{,i}+\tau_2\dot{T}_{,i})=\rho_f\ddot{u}_i+m\ddot{w}_i+\frac{\eta}{\bar{\kappa}}\dot{w}_i.
\end{aligned}
\tag{A.3}
$$

Acknowledgements The research was supported by the National Natural Science Foundation of China (Grant Nos. 42230803 and 41821002) and 111 project "Deep-Superdeep Oil & Gas Geophysical Exploration" (B18055).

References

Abouelregal AE, Marin M (2020) The size-dependent thermoelastic vibrations of nanobeams subjected to harmonic excitation and rectified sine wave heating. Mathematics 8(7):1128

Ackerman CC, Bertman B, Fairbank HA, Guyer RA (1966) Second sound in solid helium. Phys Rev Lett 16(18):789–791

Ba J, Carcione JM, Nie JX (2011) Biot-Rayleigh theory of wave propagation in double-porosity media. J Geophys Res 116(B6):1–12

Biot MA (1956) The theory of propagation of elastic waves in a fluid-saturated porous solid, I. Low-frequency range II. Higher frequency range. J Acoust Soc Am 28(182):168–191

Borcherdt RD (2009) Viscoelastic waves in layered media. Cambridge University Press

Carcione JM (2014) Wave fields in real media. Theory and numerical simulation of wave propagation in anisotropic, anelastic and porous media, 3rd ed. Elsevier

Carcione JM, Tinivella U (2000) Bottom-simulating reflectors: seismic velocities and AVO effect. Geophysics 65(1):54–67

Carcione JM, Wang ZW, Ling W, Salusti E, Ba J, Fu LY (2019a) Simulation of wave propagation in linear thermoelastic media. Geophysics 84(1):T1–T11

Carcione JM, Cavallini F, Wang E, Ba J, Fu LY (2019b) Physics and simulation of wave propagation in linear thermoporoelastic media. J Geophys Res Solid Earth 124(8):8147–8166

Corredor RM, Santos JE, Gauzellino PM, Carcione JM (2014) Reflection and transmission coefficients of a single layer in poroelastic media. J Acoust Soc Am 135(6):3151–3162

Deresiewicz H (1957) Plane waves in a thermoelastic solid. J Acoust Soc Am 29(2):204–209

Deresiewicz H (1960) Effect of boundaries on waves in a thermoelastic solid: reflexion of plane waves from a plane boundary. J Mech Phys Solids 8(3):164–172

Fu LY (2012) Evaluation of sweet spot and geopressure in Xihu (Sag. Tech. Report, CCL2012-SHPS-0018ADM): key laboratory of petroleum resource research, Institute of Geology and Geophysics, Chinese Academy of Sciences

Fu LY (2017) Deep-superdeep oil & gas geophysical exploration 111. Program report jointly initiated by MOE and SAFEA, B18055. School of Geosciences, China University of Petroleum (East China)

Green AE, Lindsay KA (1972) Thermoelasticity. J Elast 2(1):1–7

Guo J, Gurevich B (2020) Frequency-dependent P wave anisotropy due to wave-induced fluid flow and elastic scattering in a fluid-saturated porous medium with aligned fractures. J Geophys Res Solid Earth 125(8):e2020JB020320

Gurevich B, Ciz R, Denneman AIM (2004) Simple expressions for normal incidence reflection coefficients from an interface between fluid saturated porous materials. Geophysics 69(6):1372–1377

Hou W, Fu LY, Carcione JM, Wang ZW, Wei J (2021) Simulation of thermoelastic waves based on the Lord–Shulman theory. Geophysics 86(3):T155–T164

Hou W, Fu LY, Carcione JM (2022a) Reflection and transmission of thermoelastic waves in multilayered media. Geophysics 87(3):MR117–MR128

Hou W, Fu LY, Carcione JM, Han T (2022b) Reflection and transmission of inhomogeneous plane waves in thermoelastic media. Front Earth Sci 10:1–16

Hou W, Fu LY, Carcione JM (2023) Amplitude-variation-with-offset in thermoelastic media. Geophysics 88(1):MR25–MR33

Huberman S, Duncan RA, Chen K, Song B, Chiloyan V, Ding Z, Maznev AA, Chen G, Nelson KA (2019) Observation of second sound in graphite at temperatures above 100 K. Science 364(6438):375–379

Ignaczak J, Ostoja-Starzewski M (2010) Thermoelasticity with finite wave speeds. Oxford University Press

Jackson HE, Walker CT, McNelly TF (1970) Second Ssound in NaF. Phys Rev Lett 25(1):26–28

Li NQ, Fu LY, Deng WB, Carcione JM, Yang J, (2023) Coupled THM thermoelastic model for fractured-vuggy thermal reservoirs. Geophysics, in press
Li NQ, Deng WB, Fu LY, Carcione JM, Han TC (2022) Wave propagation in double-porosity thermoelastic media. Geophysics 87(6):1–40
Liu H, Dai G, Zhou F, Mu Z (2021) Propagation behavior of homogeneous plane-P1-wave at the interface between a thermoelastic solid medium and an unsaturated porothermoelastic medium. Eur Phys J Plus 136(11):1–27
Liu H, Dai G, Zhou F, Cao X (2022) A mixture theory analysis for reflection phenomenon of homogeneous plane-P 1-wave at the boundary of unsaturated porothermoelastic media. Geophys J Int 228(2):1237–1259
Lord HW, Shulman Y (1967) A generalized dynamical theory of thermoelasticity. J Mech Phys Solids 15(5):299–309
Markov M, Markova I, Pervago E (2019) Reflection and transmission of elastic waves by a fluid-filled crack located in a poroelastic formation. J Appl Geophys 167:63–72
McNelly TF, Rogers SJ, Channin DJ, Rollefson RJ, Goubau WM, Schmidt GE, Krumhansl JA, Pohl RO (1970) Heat pulses in NaF: onset of second sound. Phys Rev Lett 24(3):100–102
Nield DA, Bejan A (2006) Convection in porous media, 3rd edn. Springer
Noda N (1990) Thermal stress problem in a fluid-filled porous circular cylinder. Zeitschrift fur Angewandte Mathematik und Mechanik 70(12):543–549
Santos JE, Corbero JM, Ravazzoli CL, Hensley JL (1992) Reflection and transmission coefficients in fluid-saturated porous media. J Acoust Soc Am 91(4):1911–1923
Sharma MD (2008) Wave propagation in thermoelastic saturated porous medium. J Earth Syst Sci 117(6):951–958
Sharma MD (2018) Reflection-refraction of attenuated waves at the interface between a thermo-poroelastic medium and a thermoelastic medium. Waves Random Complex Media 28(3):570–587
Sharma MD, Kumar M (2011) Reflection of attenuated waves at the surface of a porous solid saturated with two immiscible viscous fluids. Geophys J Int 184(1):371–384
Wang E, Carcione JM, Ba J, Liu Y (2020a) Reflection and transmission of plane elastic waves at an interface between two double-porosity media: effect of local fluid flow. Surv Geophys 41(2):283–322
Wang ZW, Fu LY, Wei J, Hou W, Ba J, Carcione JM (2020b) On the Green function of the Lord-Shulman thermoelasticity equations. Geophys J Int 220(1):393–403
Wang E, Carcione JM, Yuan Y, Ba J (2021) Reflection of inhomogeneous plane waves at the surface of a thermo-poroelastic medium. Geophys J Int 224(3):1621–1639
Wei W, Zheng R, Liu G, Tao H (2016) Reflection and refraction of P wave at the interface between thermoelastic and porous thermoelastic medium. Transp Porous Media 113(1):1–27
Wei J, Fu LY, Wang ZW, Ba J, Carcione JM (2020) Green's function of the Lord–Shulman thermo-poroelasticity theory. Geophys J Int 221(3):1765–1776
Zhang L, Bhatti MM, Michaelides EE, Marin M, Ellahi R (2022) Hybrid nanofluid flow towards an elastic surface with tantalum and nickel nanoparticles, under the influence of an induced magnetic field. Eur Phys J Special Top 231(3):521–533
Zhou F, Liu H, Li S (2019) Propagation of thermoelastic waves in unsaturated porothermoelastic media. J Therm Stress 42(10):1256–1271